Volume 1 | Number 1 | Jan 2013 | Pages 1–100

Nanoscale

www.rsc.org/nanoscale

ROYAL SOCIETY
OF CHEMISTRY

This is an *Accepted Manuscript*, which has been through the Royal Society of Chemistry peer review process and has been accepted for publication.

Accepted Manuscripts are published online shortly after acceptance, before technical editing, formatting and proof reading. Using this free service, authors can make their results available to the community, in citable form, before we publish the edited article. We will replace this *Accepted Manuscript* with the edited and formatted *Advance Article* as soon as it is available.

You can find more information about *Accepted Manuscripts* in the **Information for Authors**.

ROYAL SOCIETY
OF CHEMISTRY

www.rsc.org/nanoscale

Table of Contents Entry

Highly efficient graphene-based Cu(In, Ga)Se$_2$ solar cells with large active area

Ling Yin[a,b], Kang Zhang[b], Hailin Luo[b], Guanming Cheng[b], Xuhang Ma[b], Zhiyu Xiong[b], Xudong Xiao[*,a,b]

[a]*Department of Physics, The Chinese University of Hong Kong, Shatin, Hong Kong, China*

[b]*Center for Photovoltaics and Solar Energy, Shenzhen Institutes of Advanced Technology, Chinese Academy of Sciences, Shenzhen, 518055, P. R. China*

Table of Contents Entry
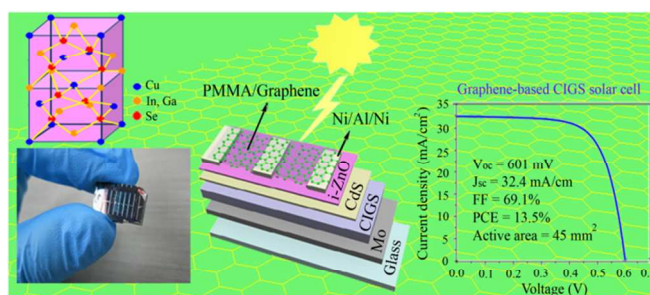
A high efficiency (13.5%) graphene-based CIGS solar cell with large active area (45 mm^2) is present.

Nanoscale

Paper

Highly efficient graphene-based Cu(In, Ga)Se₂ solar cells with large active area

Ling Yin,[a,b] Kang Zhang,[b] Hailin Luo,[b] Guanming Cheng,[b] Xuhang Ma,[b] Zhiyu Xiong[b] and Xudong Xiao[*a,b]

Two-dimensional graphene has tremendous potential to be used as transparent conducting electrode (TCE), owing to its high transparency and conductivity. Up to now graphene film has been applied to several kinds of solar cells except Cu(In, Ga)Se₂ (CIGS) solar cell. In this work, we present a novel TCE structure consisting of doped graphene film and a thin layer of Poly(methylmethacrylate)(PMMA) to replace the ZnO:Al (AZO) electrode for CIGS. By optimizing the contact between graphene and intrinsic ZnO (i-ZnO), a high power conversion efficiency (PCE) of 13.5% has been achieved, which is among the highest efficiencies of graphene-based solar cells ever reported and approaching that of AZO-based solar cell. Besides, the active area of our solar cells reaches 45 mm², much larger than other highly efficient graphene-based solar cells (>10%) reported so far. Moreover, compared with AZO-based CIGS solar cell, the total reflectance of the graphene-based CIGS solar cells is decreased and the quantum efficiency of the graphene-based CIGS is enhanced in the near infrared region (NIR), which strongly support graphene as a competitive candidate material for TCE in CIGS solar cell. Furthermore, the graphene/PMMA film can protect the solar cell from moisture, making the graphene-based solar cells much more stable than the AZO-based solar cells.

1. Introduction

ZnO:Al (AZO) films are widely used as transparent conducting electrodes (TCEs) in a-Si, CdTe, Cu(In, Ga)Se₂ (CIGS), Cu₂ZnSnS₄ (CZTS) and dye-sensitized solar cells.[1-7] However, AZO limits the photo-generated current due to rather strong absorption in the IR region of the spectrum.[1,8] Therefore new TCEs with higher transmittance beyond about 800 nm are in great need. Graphene has tremendous potential to replace AZO, owing to its high transparency with only about 2.3% absorption, absence of the thickness-dependent interference effect, and superior electrical conductivity.[9-11]

In the past few years, graphene has been widely reported as TCEs for organic photovoltaics, silicon Schottky junction and hybrid solar cells.[12-19] However, in the field of thin film solar

cells, similar work is still in its infancy. Graphene films have been used as TCEs in CdTe solar cells with a power conversion efficiency (PCE) of 4.17%.[8] The application of graphene films as window electrode in silicon thin-film solar cell has also been demonstrated.[20] However, to the best of our knowledge, there has been no report on the use of graphene-based TCEs in CIGS solar cells for replacement of AZO films. Here we present a novel TCE structure for CIGS solar cells, in which a AuCl₃ doped graphene film grown by chemical vapor deposition (CVD) was transferred with a thin layer of Poly(methyl methacrylate) (PMMA) and was then used to replace the normal AZO window layer. We have demonstrated a PCE as high as 13.5%, very close to that of the reference standard CIGS solar cell. Since the development of large area solar cell is an important step for the practical applications of solar cells, our efficiency of graphene-based solar cell with large active area of 45 mm² (13.5%) is a good achievement, and only University of Oxford and Peking University have reported higher efficiency of graphene-based solar cell (15.6% [21] and 14.5% [17]) with smaller active area (< 10 mm²) to date (as shown in Table 1S† which summarize the efficiencies of graphene-based solar cells). Researchers in Peking University also reported that their cell efficiencies would decrease from

[a] *Department of Physics, The Chinese University of Hong Kong, Shatin, Hong Kong, China E-mail: xdxiao@phy.cuhk.edu.hk*

[b] *Center for Photovoltaics and Solar Energy, Shenzhen Institutes of Advanced Technology, Chinese Academy of Sciences, Shenzhen, 518055, P. R. China*

† Electronic Supplementary Information (ESI) available. See DOI: 10.1039/b000000x/

14.5% to 10.6% with enlarging the active area of their graphene-Si solar cell by 3-fold.[17]

In this work, we employed several methods (denoted as Process A, B, C, and D in Fig. 1) to replace the AZO layer with
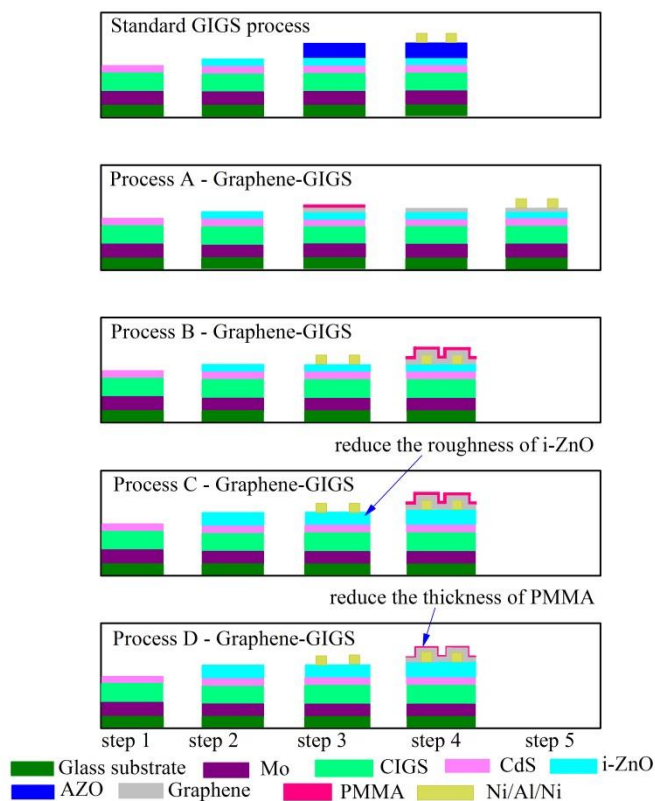
Fig. 1 (a) Schematics of the CIGS solar cell structure for various constructions: From top down, respectively, are structures of reference CIGS cell, Process A, B, C, and D cells. The differences among B, C, and D cells are noted in the figure.

graphene or graphene/PMMA layer in CIGS solar cell (see Experimental Section for details). In Process A, the AZO electrode was substituted by graphene layer while the rest layers remained the same as the CIGS reference solar cell. With the graphene/PMMA film directly transferred onto the i-ZnO surface, the PMMA was subsequently dissolved in chloroform for 10 minutes. Finally, the Ni/Al/Ni top-contact grids were deposited onto the graphene film. Compared to Process A, the position of the Ni/Al/Ni metal grids in Process B, C and D were changed from on top of the TCE to underneath the TCE, i.e., right on the i-ZnO surface. Since the cross section of the Ni/Al/Ni grids deposited by evaporation with a metal mask is trapezoidal as shown in Fig.1S†, the graphene/PMMA layer is able to conform to the surface of the i-ZnO near the Ni/Al/Ni grids. The difference between Process C and B is that the i-ZnO layer thickness in C is increased to reduce the roughness of the i-ZnO surface. Process D differs from Process C by using a thin PMMA. The active area of all the solar cells in Process A, B, C and D were determined to be 45 mm^2 by mechanical scribing,
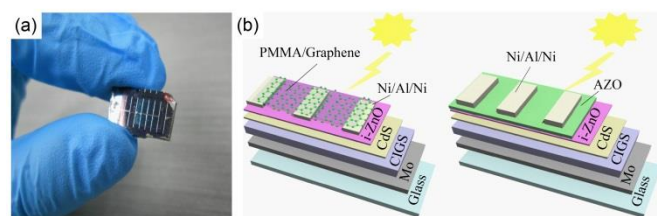
Fig. 2 (a) A photograph of a graphene-based CIGS solar cell. (b) The schematic structure of the graphene-based CIGS solar cell (left) and the reference CIGS solar cell with standard TCE structure (right)

which is much larger than other highly efficient graphene-based solar cells reported so far. Fig. 2a is a photograph of a graphene-based CIGS solar cell with novel TCE structure. Fig. 2b shows the schematic structures of the graphene-based CIGS solar cell in Fig. 2a and the reference CIGS solar cell with standard TCE structure.

2. Results and discussion

Graphene film was grown via low pressure CVD on 25μm thick Cu foil and then transferred to target substrate by using the Poly(methyl methacrylate) (PMMA) method described elsewhere.[22,23] (see Experimental Section). Fig. 3a shows the Raman spectrum of our as–grown graphene film. The Raman spectrum contains two typical peaks: the G band (~1581cm^{-1}) and the 2D band (~2683 cm^{-1}). The 2D band is a single Lorentzian peak centered at 2683 cm^{-1} with a full-width at half-maximum (FWHM) of ~ 35.4 cm^{-1}. The intensity ratio of the 2D band and the G bands (I_{2D} / I_G) is ~ 3.45, indicating that the as-grown film is single-layer graphene.[8,22] The absence of the D band indicates that our CVD grown graphene is of high quality.[22] As shown in Fig. 3b, the transmittances of 1 layer graphene is about 97.1% and is relatively flat, with little dependence on wavelength. In the same panel, the transmittances of PMMA of 150nm and 400nm thickness, 4 layer graphene, 1 layer graphene/PMMA, 4 layer graphene/ PMMA, and AZO of 150nm and 600nm thickness are shown together for comparison. Obviously, the graphene-based transparent electrodes have much better transmittance in the
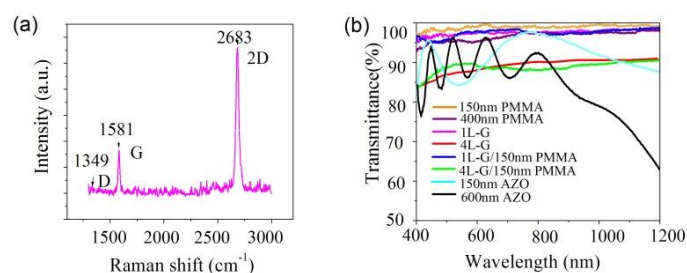
Fig. 3 (a) Raman spectrum of a monolayer graphene on SiO2/Si. (b) Transmittances of 1 layer graphene, 4 layer graphene, PMMA, 1 layer graphene/PMMA, 4 layer graphene/PMMA and AZO.

Table 1 The current density-voltage (J-V) characteristics of the reference and graphene-based CIGS solar cells fabricated by different process under AM 1.5 illumination

Samples	TCE	Process	V_{oc} (mV)	J_{sc} (mA/cm^2)	Fill factor (%)	PCE (%)
#1	150nm AZO	Reference [50 nm i-ZnO]	601	32.8	74.3	14.9
#2	1-layer G	Process A [50 nm i-ZnO]	543	0.93	25.3	0.43
#3	400nm PMMA/1-layer G	Process B [50 nm i-ZnO]	595	23.5	40.4	5.63
#4	400nm PMMA/4-layer G	Process B [50 nm i-ZnO]	596	27.4	44.2	7.20
#5	400nm PMMA/4-layer G	Process C [125nm i-ZnO]	595	31.2	56.3	10.5
#6	400nm PMMA/4-layer G	Process C [200nm i-ZnO]	603	30.1	52.2	9.50
#7	150nm PMMA/4-layer G	Process D [125nm i-ZnO]	601	32.4	69.1	13.5

wavelength range of interest as compared to the AZO films, revealing the benefits that CIGS devices made of graphene-based electrodes can enjoy.

The J-V characteristics of the reference CIGS solar cell fabricated with the standard process and the graphene-based CIGS solar cells fabricated with different Process A, B, C, and D are listed in Table 1. It is found that the CIGS solar cell with the AZO layer directly replaced by one layer graphene film in the standard solar cell structure (Mo/CIGS/CdS/i-ZnO/TCE/ Metal grid) as outlined by Process A has very low conversion efficiency, practically no current can be collected. By changing the solar cell structure and improving the adhesion between graphene and i-ZnO as outlined in Process B, C, and D, higher PCE of graphene-based CIGS solar cells have been achieved. The details are to be discussed below.

Fig. 4a and b show the optical and SEM images of the
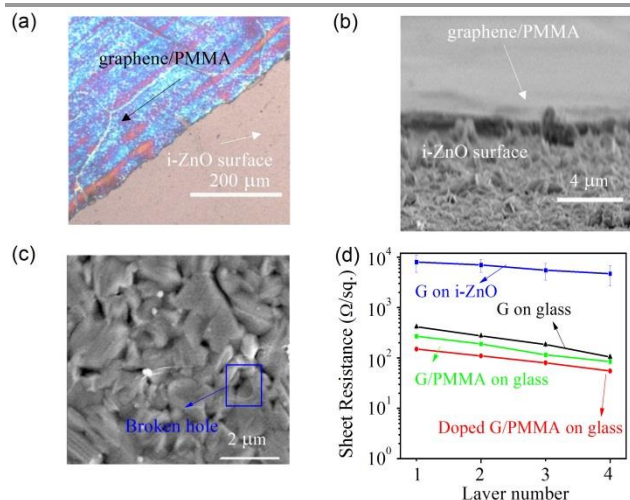
Fig. 4 (a) Optical image of a graphene-based CIGS solar cell. (b) SEM image of a graphene-based CIGS solar cell. (c) SEM image showing graphene crack on rough i-ZnO surface after PMMA removal. (d) Sheet resistance vs number of graphene layers for graphene on i-ZnO, glass, and PMMA substrates. AuCl$_3$ doped graphene is also shown for comparison.

surface of a CIGS solar cell with the graphene/PMMA film directly transferred onto the i-ZnO layer (for the case of Process A in Fig.1). It is clear that the graphene/PMMA film at this stage does not exhibit any dilapidation due to the mechanical protection of PMMA. However, when the PMMA is removed by chloroform, many small cracks and holes start to appear in the graphene layer due to the surface roughness of i-ZnO, as demonstrated in Fig. 4c. As the transparent conducting electrode of the CIGS solar cell with large active area, a graphene layer with such high density of cracks presents a very high sheet resistance (R_{sheet}), resulting in high series resistance (R_s) of the solar cells (Fig. 4d). Moreover, the cracks in graphene and the residual of PMMA are harmful for current collection since they jeopardize the quality of the deposited Ni/Al/Ni grids. This explains the very low power conversion efficiency (PCE<0.5%) from the first graphene-based CIGS solar cell (sample #2) in Table 1 fabricated by Process A.

To eliminate the above problems, we have designed a new structure of the graphene-based CIGS solar cell without removing the PMMA layer. As presented for Process B in Fig. 1, the Ni/Al/Ni grid was deposited onto the i-ZnO layer prior to the transfer of the graphene/PMMA film. As shown in Fig. 3b, the PMMA layer with either 150 nm or 400 nm thickness is perfectly transparent. Without removal of PMMA (Fig. 4d), the 1-layer graphene/PMMA has a sheet resistance of 272 Ω/sq, while the graphene film on glass substrate after removal of PMMA has a much higher sheet resistance of 415 Ω/sq. The sheet resistance of the graphene/PMMA film decreases with the increase of the number of graphene layers. 4-layer graphene/PMMA has a low sheet resistance of 87 Ω/sq. In contrast, when the as-grown graphene film was transferred to 125 nm thick i-ZnO layer and the PMMA was subsequently removed, its sheet resistance increases by at least one order of magnitude compared with the graphene transferred to a flat glass substrate after the remove of PMMA. This suggests that the rough i-ZnO surface is detrimental to the conductivity of graphene, consistent with the SEM observations in Fig. 4c.

To further decrease the sheet resistance, the graphene/PMMA films were immersed in 20 mM $AuCl_3$ aqueous solution for 30 s for doping before transferred to the i-ZnO surface. After doping, the sheet resistance of 4-layer graphene/PMMA is reduced from 87 to 55 Ω/sq while the transmittance of the whole film remains about 89% at 550 nm. These results are much better than most of the reported graphene based TCEs and are close to the best result ever reported.[24]

As revealed in Table 1, using doped graphene/PMMA films as TCE in the graphene-based CIGS solar cells and the fabrication Process B, the cell performance is significantly improved with a much higher current density than that from cells made by Process A. As shown in Fig. 2S† and Table 1, the solar cell with 4-layer graphene TCE (sample #4) exhibits a much better performance with a power conversion efficiency of 7.20%, while the 1-layer graphene solar cell (sample #3) has an efficiency of 5.62%. The difference in the conversion efficiency for the 1-layer and 4-layer graphene TCE solar cells comes both from their current density and fill factor. With more graphene layers, the sheet resistance is reduced and the electron charge collection by the TCE is improved, resulting in a higher current density and a larger fill factor. However, the increase of the number of graphene layers reduces the light transmittance and jeopardizes the advantage of graphene in its transparency and therefore the final conversion efficiency of CIGS solar cells.

However, graphene-based solar cells made by Process B are still much inferior to the reference CIGS solar cell, mostly in terms of the current density and the fill factor. By comparing the structure of the graphene-based CIGS solar cell and the standard CIGS solar cell (Fig. 1), we found two possible reasons: 1. The sheet resistance of the 4-layer graphene/PMMA film (about 55 Ω/sq) is still higher than that of 150 nm AZO (about 20-30 Ω/sq); 2. The contact between graphene and i-ZnO is still not good enough for effective electron charge transfer. While it is difficult to reduce the sheet resistance of graphene layers at this stage, the contact between graphene and i-ZnO surface can be improved.

We here use a model to illustrate how the i-ZnO/TCE interface influences the performance of the CIGS solar cells, as sketched in Fig. 5a. The solar cell has a textured interface due to the inherent structures of CIGS, CdS and i-ZnO. The contact morphology between graphene and i-ZnO can lead to three types of cells: Cell-A, Cell-B and Cell-C. We use θ to represent the difference of the contact morphology dictated by the i-ZnO surface. For Cell-A, θ equals to180°, implying a flat interface. For Cell-B and Cell-C, θ is in the range of 0°~180° and $θ_B$ is larger than $θ_C$. In the case of AZO/CIGS solar cells, since the AZO TCE is deposited by RF sputtering, it uniformly covers the whole i-ZnO surface independent of the detailed morphology. In the case of graphene-based CIGS solar cells, since the graphene/PMMA TCE is transferred to the i-ZnO surface by wet transfer method, the graphene/PMMA cannot fully conform to the i-ZnO surface if θ is very small, as depicted in Cell-C by Fig. 5a. In contrast, for θ much bigger

than 0°, the graphene/PMMA is flexible to develop large enough bending to conform to the substrate, as modelled by
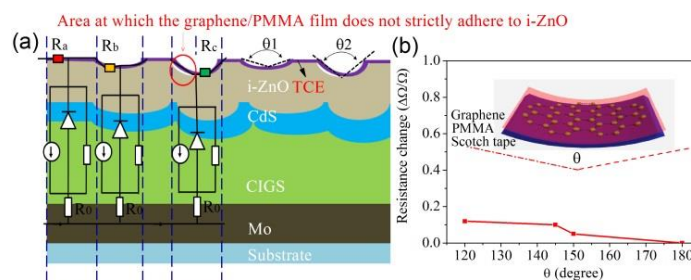
Fig. 5 (a) Schematic drawing of three kinds of interface between graphene/PMMA and i-ZnO. (b) Resistance change as a function of the bending angle of graphene/PMMA. The inset shows a schematic image of the curved graphene/PMMA/Scotch tape.

Cell-A and Cell-B in Fig. 5a. We use a single diode model to analyse the performance in Cell-A, Cell-B and Cell-C for the graphene-based CIGS solar cells. As illustrated in Fig. 5a, the J-V characteristics can be described by

$$J = J_0 \exp[\frac{q}{AKT}(V - R_s J) - 1] + \frac{V - R_s J}{R_{sh}} - J_L$$

where J_0 is the reverse saturation current, J_L is the photo-current, q is the electron charge, A is the ideality factor, k is the Boltzmann constant, T is the temperature, R_s is the series resistance, and R_{sh} is the shunt resistance.

The series resistance can be expressed by $R_s = R_0 + R$. Here R_0 consists of (1) bulk resistance of the function layers of the solar cell, (2) bulk resistance of the back electrode, and (3) contact resistance of all the interfaces except the interface between graphene/PMMA and i-ZnO in the device. The resistance R refers to the bulk resistance of graphene/PMMA film and the contact resistance between graphene/PMMA and i-ZnO. For Cell-A, Cell-B and Cell-C, R is given by R_a, R_b, and R_c respectively. At different bending, as shown in Fig. 5b, the bulk resistance of graphene/PMMA film decreases with the increase of θ. This phenomenon was also observed in many other work.[24,25,26] Therefore, R_a of Cell-A is smaller than R_b in Cell-B, and thus in principle the conversion efficiency of Cell-A is higher than that of Cell-B. The reason for larger R_c than R_b is not only from the bulk resistance contribution of the graphene/PMMA film, but more importantly also from the contribution due to the incomplete contact between graphene/PMMA film and the i-ZnO surface.

The above analysis suggests that the poor interface between the graphene TCE and the i-ZnO surface is an important cause for the low efficiency of graphene-based CIGS solar cell. Below, we demonstrate two strategies to modify this interface. Either by optimizing the thickness of i-ZnO as in Process C or by reducing the PMMA thickness in the transfer process of graphene as in Process D, a better contact between graphene

and i-ZnO and thus a higher efficiency of the graphene-based CIGS solar cell can be achieved.
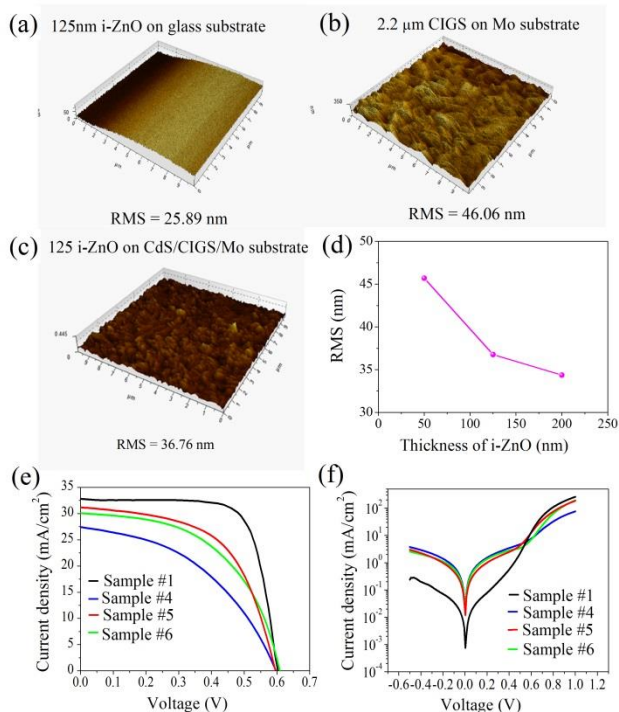
Fig. 6 (a) AFM image of 125nm i-ZnO on glass substrate. (b) AFM image of CIGS (2.2um) on Mo substrate. (c) AFM image of 125nm i-ZnO on CdS/CIGS (2.2um)/Mo substrate. (d) i-ZnO RMS roughness as a function of i-ZnO film thickness when deposited on CdS/CIGS/Mo samples. (e) The J-V curves of the graphene-based CIGS solar cells with different thickness of i-ZnO films under AM1.5 illumination. (f) The dark J-V curves of graphene-based CIGS solar cells with different thickness of i-ZnO films.

As we discussed above, the surface morphology of i-ZnO plays an important role in the contact with the graphene/PMMA film. As shown in Fig. 6a and Fig. 6c, the root-mean-square (RMS) roughness of the 125 nm thick i-ZnO deposited on a glass substrate is only about 25.9 nm, but increases to 36.8 nm if deposited on the CdS/CIGS/Mo substrate. This result indicates that the higher roughness of i-ZnO/CdS/CIGS/Mo is mainly caused by the CIGS film (RMS=46.06 nm), as shown in Fig. 6b. Nevertheless, it is found that the RMS roughness of i-ZnO films on CdS/CIGS/Mo decreases as the thickness of i-ZnO increases. As shown in Fig. 6d, the RMS roughness of i-ZnO films decreases from 45.70 to 34.36 nm as the thickness increases from 50 nm to 200 nm.

Base on the above observation, we designed Process C in which the thickness of i-ZnO was varied from 50 to 200 nm to optimize graphene based CIGS solar cells. As shown in Fig. 6e and Table 1, when the thickness of i-ZnO is increased from 50 to 125 nm, both J_{sc} and FF of the graphene based solar cells increase substantially. Further increase of the i-ZnO thickness to 200 nm resulted a small decrease of the conversion efficiency, but still a better performance than the 50 nm thick i-ZnO solar cell. We attribute the increase of J_{sc} and FF mainly to the much smoother surface of i-ZnO film, which leads to a better contact with the graphene/PMMA film. As the roughness becomes smaller with the i-ZnO thickness increase from 50 to 125 nm, θ would increase and the percentage of Cell-C in the graphene based CIGS solar cell would decrease which improves the overall J_{sc} and FF of the whole solar cell. For the solar cell with 200 nm thick i-ZnO film, although the surface becomes even flatter with a RMS roughness of 34.36 nm, slight drops in J_{sc} and FF are observed, possibly due to the higher bulk resistance of the thicker i-ZnO film.

To assist our analyses, we also measured the dark J-V curves of these graphene-based CIGS solar cells as showed in Fig. 6f. The dark J-V curves can be fitted by Eq. (1) with $J_L=0$. The fitting parameters are summarized in Table 2. It can be seen that R_s is reduced and R_{sh} is enhanced when the thickness of i-ZnO is increased from 50 to 125 (or 200 nm). This perfectly explains the increase of FF in the graphene-based CIGS solar cells with relatively thick i-ZnO film. Possibly due to the higher sheet resistance of graphene film and the poorer contact between graphene and i-ZnO, the R_s and R_{sh} of the graphene based CIGS solar cells are respectively about two times larger and a few times smaller than those of the reference AZO-CIGS solar cell, respectively, resulting in smaller J_{sc} and FF obtained for the graphene-based CIGS solar cells.

Since the graphene-based CIGS solar cell with 125 nm i-ZnO layer has higher conversion efficiency, in the following, the 125 nm thick i-ZnO was chosen in the subsequent experiments for better performance.

To further increase the efficiencies of graphene/PMMA based CIGS solar cells, the transfer process of graphene film was optimized as shown in Process D (Fig. 1). In order to make the graphene/PMMA film conform to the i-ZnO better,

Table 2 The fitted current density-voltage (J-V) characteristics of the reference and graphene -based CIGS solar cells.

Samples	TCE	Process	R_s ($\Omega \cdot cm^2$)	R_{sh} ($\Omega \cdot cm^2$)	A	J_0 (mA/cm²)
#1	150nm AZO	Reference [50 nm i-ZnO]	0.84	5440	1.92	$8.90*10^{-6}$
#4	400nm PMMA/4-layer G	Process B [50 nm i-ZnO]	3.45	141	2.05	$1.69*10^{-4}$
#5	400nm PMMA/4-layer G	Process C [125 nm i-ZnO]	1.70	221	1.97	$1.24*10^{-4}$
#6	400nm PMMA/4-layer G	Process C [200 nm i-ZnO]	1.13	161	1.93	$2.25*10^{-5}$
#7	150nm PMMA/4-layer G	Process D [125nm i-ZnO]	0.97	3125	1.91	$4.30*10^{-5}$

we attempted to make the composite film softer by decreasing the thickness of PMMA and eliminating the baking process of PMMA. Here, we controlled the thickness of PMMA by the rotating speed of spin-coating and obtained a minimum thickness of 150 nm. In addition, we dried the PMMA in air at room temperature for 30 minutes instead of baking it at 120°C for 10 minutes.

From the J-V characteristics shown in Fig. 7a and Table 1, it can be found that great improvements have been achieved for the solar cell fabricated by process D. The PCE of sample #7 was as high as 13.5% with V_{oc} of 601mV, J_{sc} of 32.4mA/cm^2, and FF of 69.1%, very close to that of the reference cell (sample #1, PCE, 14.9% with V_{oc}, 601mV, J_{sc}, 32.8mA/cm^2; and FF, 74.3%). In contrast, the solar cell with 400 nm PMMA on graphene as the transparent electrode (sample #5) showed relatively poor cell performance (PCE, 10.5%; V_{oc}, 595mV; J_{sc}, 31.2 mA/cm^2 and FF, 52.2%). The R_s and R_{sh} of graphene-based CIGS solar cell fabricated by Prcocess D were also improved as shown in Table 2. The higher PCE for sample #7 could be attributed to the improved interface between the rough i-ZnO surface and the graphene/PMMA film, since the thinner PMMA was much softer and could result in better surface contact with easy conformity. Fig. 7b displays the photo of sample #5 and sample #7 without metal grid (the metal grid was not applied here for the precise measurement of the reflectance in Fig. 8). It is clearly shown that the color of sample #7 is darker than that of sample #5. In addition, when we put the two samples into water or scribed them to determine the active area, the graphene/PMMA TCE film of samples #5
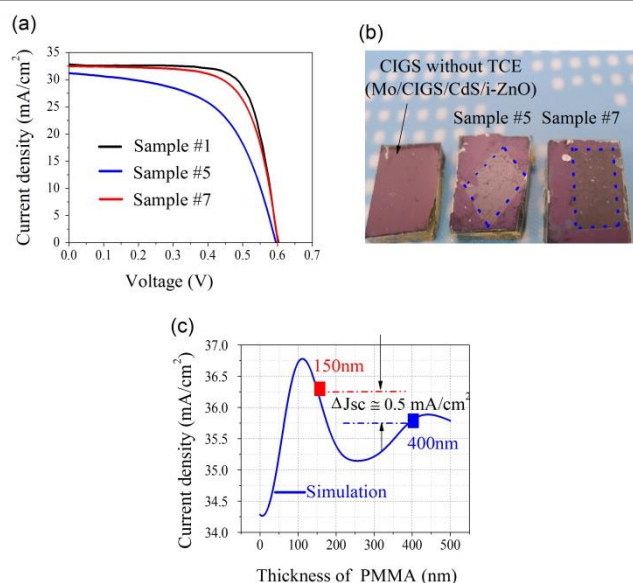
was found to be easy to peel off the i-ZnO film, while no such phenomenon was found for sample #7, which also proves the better contact in sample #7. The high J_{sc} of sample #7 could also be partially attributed to the anti-reflection effect by the thin PMMA according to the simulation results shown in Fig. 7c.

Compared with CIGS solar cell with standard AZO as TCE, though the PCE of graphene-based CIGS solar cell is slightly lower due to the lower J_{sc} and FF, the graphene-based CIGS solar cell is found to exhibit excellent optical and electrical properties. Firstly, due to the refractive index matching and the anti-reflection effect of graphene/PMMA films, the total reflectance of grahene-based CIGS solar cell (sample #7) is lower than that of standard CIGS solar cell as shown in Fig. 8. Secondly, the EQE result demonstrates the potential of utilizing graphene film to replace AZO films as the window layer in CIGS solar cell to improve the quantum efficiency in the NIR. As shown in Fig. 9, the dQE/dλ curves showed the function layers (ZnO, CdS, CIGS) are the same in graphene-based CIGS solar cell and standard AZO-based CIGS solar cell, while the normalized EQE of the graphene-based CIGS solar cell is slightly higher than that of the AZO-based CIGS solar cell in
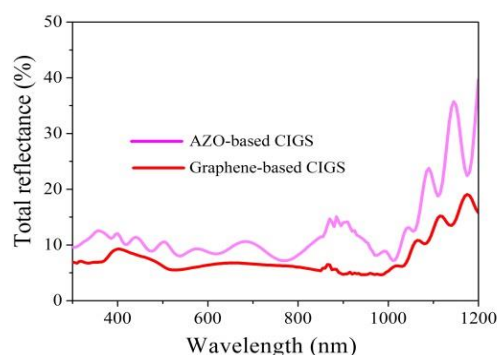
Fig. 8 Reflectance spectrum of graphene-based CIGS solar cells (sample #7) and standard AZO-based CIGS solar cell.
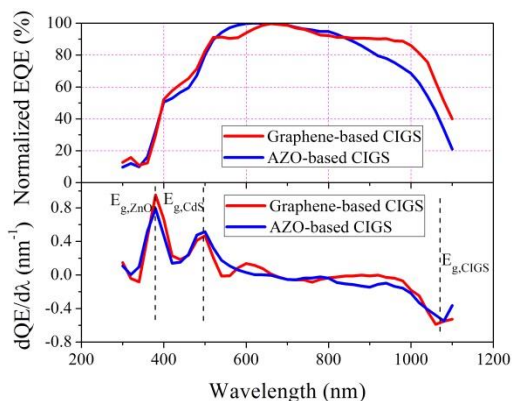
Fig. 9 Normalized external quantum efficiency (EQE) of graphene-based CIGS (sample #7) and AZO-based CIGS solar cell.

Fig. 7 (a) The J-V curves of graphene-based CIGS solar cells with different PMMA thickness under AM1.5 illumination. (b) Image of CIGS solar cell without TCE, graphene-based CIGS solar cells (sample #5 and sample #7) without Ni/Al/Ni metal grid. (c) Simulated current density of graphene-based CIGS solar cells with different PMMA thickness.

NIR, which is caused by the high transmission of the graphene TCE films in the NIR due to the low free carrier absorption loss.

It is well known that AZO is susceptible to moisture in air, while graphene possesses excellent chemical stability. Moreover, graphene is nearly impermeable to any gas and liquid, therefore it can protect the solar cell from moisture.[27-29] The stability of the graphene-based CIGS solar cell was examined in air at temperature of 25°C and humidity of 45%. For comparison, the reference CIGS solar cell was put in the same room and characterized under the same conditions. Fig. 3S† shows the normalized PCE of the devices after different periods. After 83 days, the loss in PCE for the graphene-based CIGS solar cell is around 3% while for the reference CIGS solar cell is around 9%. Moreover, this passivation effect of grahene in graphene-based CIGS solar cell is also an advantage for encapsulated CIGS solar cells. The acetic acid from encapsulation material (EVA) is reported to be an important factor which leads to the degradation of traditional encapsulated CIGS solar cell, [30] while with graphene preventing the solar cell from acetic acid, this problem can be avoided.

3.   Conclusions

In summary, we have demonstrated that CVD grown graphene film with a thin layer of PMMA coating can efficiently serve as the transparent conducting electrode for CIGS solar cells to replace AZO. With a set of progressively improved processes to achieve better interface contact between the graphene/PMMA and i-ZnO layers, a high PCE of 13.5% has been achieved, which is remarkable for large active area up to 45 mm^2. Besides, graphene-based CIGS solar cell exhibits excellent optical and electrical properties such as lower total reflectance and enhanced quantum efficiency in the NIR compared with standard AZO-based CIGS solar cell. Furthermore, due to the protection of the PMMA/ graphene film, the graphene-based solar cell shows better stability than the standard AZO based solar cell, and this advantage could also be meaningful for encapsulated CIGS solar cell. With more effort in reducing the sheet resistance of graphene, higher PCE of graphene-based CIGS solar cell is possible. Our experiments presented in this work shall be regarded as the first attempt in this direction and hopefully will attract further research in the future.

4.   Experimental section

Synthesis of monolayer graphene

Graphene film was grown via low pressure CVD on 25μm thick Cu foil (Alfa Aesar, Product No.46365) in a quartz tube placed in a three-zone horizontal tube furnace (Lindberg/blue HTF55667C). At first, the Cu foil was treated with Ethyl lactate for 1 hour and then rinsed with isopropyl and DI water. Then the Cu foil was annealed in the CVD chamber at 1035°C for 30 minutes. After that, 2 sccm CH_4 along with 30 sccm H_2 were introduced for 18 minutes. Then the flow rate of CH_4 was increased to 20 sccm for 2 minutes. Finally, the Cu substrate was cooled to 200 °C under CH_4:H_2=5:30 sccm.

Graphene transfer and doping technique

To transfer the as-grown graphene film, a thin layer of PMMA was spin-coated on the sample. The copper substrate was then etched away by $FeCl_3$ solution (1mol/L) for 1 hour with the graphene layer on the back side of the Cu substrate removed prior in O_2 plasma. To reduce the sheet resistance of graphene, the graphene/PMMA film was immersed in 20mM $AuCl_3$ aqueous solution for 30s and then thoroughly washed with DI water. In the case of multilayer graphene films, a layer-by-layer transfer method was used in which the previous graphene/PMMA film was placed conformally on top of another graphene/Cu layer, followed by etching away the Cu substrate.

Fabrication of CIGS reference solar cell

The fabrication process of the reference CIGS solar cell with the standard AZO electrode can be briefly described as follows: A 1μm Mo back contact film was first deposited by DC-magnetron sputtering on a 2 mm thick soda-lime glass substrate at room temperature. Then, a 2-3μm CIGS absorber layer was grown by the three-stage process using a co-evaporation deposition system. The CdS buffer layer was deposited on top of the absorber via chemical-bath deposition method. Afterwards, a high resistivity intrinsic ZnO (i-ZnO) layer was deposited at room temperature in Ar and O_2 atmosphere from an intrinsic ZnO target, followed by a ~150 nm thick AZO film deposited by RF-sputtering from an AZO target. Finally, Ni/Al/Ni metallic grids with a thickness of about 8μm were fabricated on top of the AZO by electron beam evaporation.

Fabrication of graphene-based CIGS solar cell with standard structure (Process A)

In Process A, the AZO electrode was substituted by graphene layer while the rest layers remained the same as the CIGS reference solar cell. With the graphene/PMMA film directly transferred onto the i-ZnO surface, then the solar cell was annealed at 100 °C for 10 min to enhance the adhesion between graphene and i-ZnO. The PMMA was subsequently dissolved in chloroform for 10 minutes. Finally, the Ni/Al/Ni top-contact grids were deposited onto the graphene film.

Fabrication of graphene-based CIGS solar cell with PMMA as protection and antireflection layer (Process B, C and D)

Compared to Process A, the position of the Ni/Al/Ni metal grids in Process B, C and D were changed from on top of the TCE to underneath the TCE, i.e., right on the i-ZnO surface. The graphene/PMMA layer was then directly laminated on top of Ni/Al/Ni metal grids, contacting both Ni/Al/Ni and i-ZnO. The solar cell was annealed at 100 °C for 10 min to enhance the adhesion between graphene and i-ZnO or Ni/Al/Ni metal grid. The difference between Process C and B is that the i-ZnO layer thickness in C is increased to reduce the roughness of the i-ZnO surface. Process D differs from Process C by using a thin PMMA.

Material and device characterizations

The morphologies of the solar cells were characterized by scanning electron microscopy (SEM), atomic force microscopy (AFM), and optical microscopy (OM). The visible-IR spectra were obtained by a spectrophotometer with a wavelength range from 300 nm to 1200 nm. The sheet resistances of the graphene films were measured via the Van Der Pauw method. The J–V measurements of the solar cells were performed under dark or with illumination of the standard AM1.5 spectrum with 100mW/cm^2 at 25°C. The intensity of the light source of the solar simulator was calibrated with a standard single crystal Si solar cell. The EQE of the solar cells were measured with a standard system equipped with a xenon lamp, a monochromator, a Si detector, and a dual channel power meter. The active area of solar cells was determined to be 45 mm^2 by mechanical scribing.

Acknowledgements

Notes and references

1 H. Y. Liu, V. Avrutin, N. Izyumskaya, Ü. Özgür and H. Morkoç, *Superlattices and Microstructures*, 2010, **48**, 458–484.

2 F. H. Wang, H. P. Chang, C. C. Tseng, C. C. Huang and H. W. Liu, *Current Applied Physics*, 2011, **11**, S12-S16.

3 A. Crossay, S. Buecheler, L. Kranz, J. Perrenoud, C. M. Fella, Y. E. Romanyuk and A. N. Tiwari, *Solar Energy Materials and Solar Cells* 2012, **101**, 283-288.

4 Y. K. Liao, Y. C. Wang, Y. T. Yen, C. H. Chen, D. H. Hsieh, S. H. Chen, C. Y. Lee, C. C. Lai, W. C. Kuo, J. Y. Juang, J, Y, K. H. Wu, S. J. Cheng, C. H. Lai, F. I. Lai, S. Y. Kuo, H. C. Kuo and Y. L. Chueh, *ACS Nano,* 2013, **7(8)**, 7318-7329.

5 S. Rampino, N. Armani, F. Bissoli, M. Bronzoni, D. Calestani, M. Calicchio, N. Delmonte, E. Gilioli, E. Gombia, R. Mosca, L. Nasi, F. Pattini, A. Zappettini and M. Mazzer, *Appl. Phys. Lett.,* 2012, **101**, 132107-1-4.

6 L. Rovelli, SD. Tilley and K. Sivula, *ACS Appl Mater Interfaces*, 2013, **5(16),** 8018-8024.

7 S. H. Lee, S. H. Han, H. S. Jung, H, Shin, J. Lee, J. H. Noh, S. Lee, I. S. Cho, J. K. Lee, J. Kim and H. J. Shin, *Chem. C,* 2010, **114**, 7185–7189.

8 H. Bi, F. Q. Huang, X. M. Xie and M. H. Jiang, *Adv. Mater.,* 2011, **23**, 3202-3206.

9 X. Li, Y. Zhu, W. Cai, M. Borysiak, B. Han, D. Chen, R. D. Piner, L. Colombo and R. S. Ruoff, *Nano Lett.,* 2009, **9**, 4359-4363.

10 W. Wu, Q. K. Yu, P. Peng, Z. H. Liu, J. M. Bao and S. S. Pei, *Nanotechnology*, 2012, **23**, 035603.

11 R. R. Nair, P. Blake, A. N. Grigorenko, K. S. Novoselov, T. J. Booth, T. Stauber, N. M. R. Peres and A. K. Geim, *Science*, 2008, **320**, 1308.

12 Z. Y. Yin, J. X. Zhu, Q. Y. He, X. H. Cao, C. L. Tan, H. Y. Chen, Q. Y. Yan and H. Zhang, *Adv. Energy Mater.,* 2013, **4**, 1300574.

13 Z. K. Liu, J. H. Li, Z. H. Sun, G. A. Tai, S. P. Lau and F. Yan, *ACS Nano*, 2012, **6**, 810-818.

14 H. Park, R. P. Brown, V. Bulović and J. Kong, *Nano Lett.*, 2012, **12**, 133−140.

15 X. M. Li, H. W. Zhu, K. L. Wang, A. Y. Cao, J. Q. Wei, C. Y. Li, Y. Jia, Z. Li, X. Li and D. H. Wu, *Adv. Mater.*, 2010, **22**, 2743–2748.

16 X. C. Miao, S. Tongay, M. K. Petterson, K. Berke, A. G. Rinzler, B. R. Appleton and A. F. Hebard, *Nano Lett.*, 2012, **12**, 2745−2750.

17 E. Z. Shi, H. B. Li, L. Yang, L. H. Zhang, Z. Li, P. X. Li, Y. Y. Shang, S. T. Wu, X. M. Li, J. Q. Wei, K. L. Wang, H. W. Zhu, D. H. Wu, Y. Fang and A. Y. Cao, *Nano Lett.,* 2013, **13 (4)**, 1776–1781.

18 H. Park, S. Chang, J. Jean, J. J. Cheng, P. T. Traujo, M. S. Wang, M. G. Bawendi, M. S. Dresselhaus, V. Bulovic, J. Kong and S. Gradecak, *Nano Lett.,* 2013, **13**, 233-239.

19 Y. Wang, S. W. Tong, X. F. Xu, B. Özyilmaz and K. P. Loh, *Adv. Mater.*, 2011, **23**, 1514–1518.

20 R. Ishikawa, M. Bando, H. Wada, Y. Kurokawa, A. Sandhu and M. Konagai, Japanese Journal of Applied Physics, 2012, **51**, 11PF01-1-4.

21 J. T. W. Wang, J. M. Ball, E. M. Barea, A. Abate, J. A. Webber, J. Huang, M. Saliba, M. S. Iván, J. Bisquert, H. Snaith and R. J. Nicholas, *Nano Lett.*, 2014, **14(2)**, 724-730.

22 X. S. Li, W. W. Cai, J. H. An, S. Kim, J. Nah, D. X. Yang, R. Piner, A. Velamakanni, I. Jung, E. Tutuc, S. K. Banerjee, L. Colombo and R. S. Ruoff, *Science,* 2009, **324**, 1312-1314.

23 A. Reina, X. T. Jia, J. Ho, D. Nezich, H. B. Son, V. Bulovic, M. S. Dresselhaus and J. Kong, *Nano Lett.,* 2009, **9 (1)**, 30-35.

24 S. Bae, H. Kim, Y. Lee, X. F. Xu, J. S. Park, Y. Zheng, J. Balakrishnan, T. Lei, H. R. Kim, Y. I. Song, Y. J. Kim, K. S. Kim, B. Ozyilmaz, J. H. Ahn, B. H. Hong and S. Iijçima, *Nature Nanotechnol*, 2010, **5**, 574-578.

25 Y. U. Jung, S. I. Oh, S. H. Cho, H. K. Kim and S. J. Kang, *Current Applied Physics*, 2013, **13**, 1331-1334.

26 J. Y. Hong, K. Y. Shin, O. S. Kwon, H. Kanga and J. Jang, *Chem. Commun.*, 2011,**47**, 7182-7184.

27 V. Berry. *Carbon*, 2013, **62**, 1-10.

28 Y. D. Zhao, Y. Z. Xie, Y. Y. Hui, L. B. Tang, W. J. Jie, Y. F. Jiang, L. Xu, S. P. Laua and Y. J. Chai, *Mater. Chem. C*, 2013,**1**, 4956-4961.

29 R. R. Nair, H. A. Wu, P. N. Jayaram, I. V. Grigorieva and A. K. Geim, *Science*, 2012, 442-444.

30 P. O. Westin, P. Neretnieks and M. Edoff, *Proceedings of the 21st European Photovoltaic Solar Energy Conference*, 2006, 2470-2473.

Nanoscale Accepted Manuscript